Published in: Journal of Applied Physics https://aip.scitation.org/journal/jap
Volume: 126 **Issue:** 16 **Article Number:** 165302 **DOI:** 10.1063/1.5115823 **Published:** OCT 28 2019

For personal use only

Role of the electron-phonon coupling on the thermal boundary conductance of metal/diamond interfaces with nanometric interlayers

Maïté Blank[1*], Gionata Schneider[1], Jose Ordonez-Miranda[2] and Ludger Weber[1,3]

[1]*Laboratory of Mechanical Metallurgy, Ecole Polytechnique Fédérale de Lausanne, CH-1015 - Lausanne, Switzerland*

[2]*Institut Pprime, CNRS, Université de Poitiers, ISAE-ENSMA, F-86962 Futuroscope Chasseneuil, France*

[3]*Now with TAGHeuer Institute, Rue Louis-Joseph Chevrolet 6A, CH-2300 La Chaux-de-Fonds, Switzerland*

* *Corresponding author: maite.blank@epfl.ch*

ABSTRACT

Thermal Boundary Conductance (TBC) of the Ag/diamond and Au/diamond interfaces with a nanometer-thick interface layer of either nickel or molybdenum is measured by Time Domain Thermoreflectance (TDTR) and modelled based on a 3-layer two-temperature model (3l-TTM). The rationale for this study is to critically assess the role of the electron-phonon coupling factor of the interlayer along with its thickness on the TBC. It is shown that the TBC of both systems rapidly increases with the interlayer thickness until reaching a stable plateau for thicknesses greater than 1.5 nm. The plateau average value is 15-25% lower than the intrinsic TBC between the interlayer material and the diamond substrate. This behaviour and values of the TBC of both systems are in good agreement with the predictions of the 3l-TTM. The predictability of this model is also analysed for a Cu interlayer inserted at Au/silicon interfaces with thicknesses ranging from 1.5 to 20 nm. While the room temperature TBC of this system is well described by the 3l-TTM, the values measured at 80 K can only be predicted by the 3l-TTM, provided that the interlayer electron-phonon coupling factor is reduced by a factor 2, as was experimentally observed for Ag and Au. The obtained experimental results along with the proposed model can thus be useful for tailoring the TBC of metallic interfaces in a wide range of temperatures.

I. INTRODUCTION

With the continuous miniaturization of devices with enhanced rates of operation, the efficient management of heat transfer has become very challenging, due to the overheating, low reliability, and reduced lifetimes of the involved nanomaterials. One of the key parameters driving the thermal performance of these devices is the finite TBC (h_{BD}) between their different components, whose interfaces usually exhibit temperature jumps ΔT given by $\Delta T= J \cdot h_{BD}$, with J being the heat flux across them. Typical values of the TBC for metal/dielectric interfaces are in the range of (10 – 800) MW/m^{2}K, (1), and its importance can conveniently be evaluated through the ratio $h_{BD} \cdot d/\kappa$ between the product $h_{BD} \cdot d$ and the bulk thermal conductivity (κ) of the interlayer material of thickness d. This ratio is similar to the Biot number in macroscopic heat transfer and indicates that the interface becomes progressively the main resistance to the heat flow for $h_{BD} \cdot d/\kappa \leq 1$, which is, for example, often the case in laser diodes (2). This is the reason why extensive research efforts were carried out for enhancing the TBC, whose values are determined by the materials on either side of the interface (1,3) and increase with the strength of the interfacial bonding (4–6) and/or by reducing the interfacial roughness (7–9).

In order to tailor the values of the TBC between a metallic film and its substrate, the influence of a thin interlayer with bridging properties inserted at their interface was studied in several works. By inserting Ti interlayers at both Al/graphite (10) and Au/Si (11) interfaces, the TBC was significantly enhanced, which was attributed to an improved interfacial bonding. Similarly, Wang *et al*. (12) observed that Al and Pt interlayers with thicknesses ranging from 10 to 100 nm are able to enhance the TBC of Au/Si interfaces, which was attributed to the electron-phonon coupling strengthening. Based on much thinner (0.3 to 8 nm) interlayers of copper and chromium inserted at the Au/Al_2O_3 interface, Jeong *et al*. (13) showed that the TBC monotonously increases with the interlayer thickness, before reaching a plateau. Similar results were recently observed by our group (14) for copper interlayers (1.5-20 nm) inserted at the Au/Si, Au/Al_2O_3 and Au/diamond interfaces. The interpretation of the physical mechanisms generating this TBC behaviour was, however, slightly different in both cases. By assuming that the interlayer contribution to the overall thermal transport across the interface is determined by phonons with wavelengths smaller than its thickness, Jeong *et al.* (13) fitted a modified Diffuse Mismatch Model (DMM) to their experimental results. By contrast, our results were described by means of an thermal resistance generated by the electron-phonon coupling inside the interlayer (14). This additional resistance decreases as the interlayer thickness increases, such that the higher the electron-phonon coupling, the thinner the interlayer thickness required to reach the TBC plateau.

The purpose of this work is to rigorously assess this latter statement by measuring and modelling the TBC of metal/dielectric interfaces with ultra-thin interlayers involving

strong and weak electron-phonon coupling. This is done by comparing the experimental TBC values to the theoretical predictions of the simplified model presented in Ref. (14) and a refined one based on the two-temperature model applied to a three-layers system (3l-TTM). This analytical 3l-TTM explicitly takes into account the effect of the interlayer thickness on the TBC and its predictions are in good agreement with various experimental data even at 80 K, provided that the interlayer electron-phonon coupling is reduced by a factor of two with respect to its value at room temperature.

II. EXPERIMENTAL METHOD

a. Sample preparation and characterization

Ag-Ni-diamond, Au-Ni-diamond and Ag-Mo-diamond stacks were all fabricated by following the procedure developed for Au-Cu-diamond stacks and presented in our previous work (14). All diamond substrates consisted of HPHT synthetic stones (Ref: MWS L25 with [100] orientation, purchased from Element 6, Shannon, Co. Clare, Ireland) and their surface state was controlled through a succession of mechanical polishing steps (6 μm, 3 μm, and 1 μm diamond paste) followed by ultrasonic cleaning in acetone, ethanol and isopropanol. Surface activation was achieved by using a Fischione 1020 oxygen plasma cleaner with a 3:1 Ar:O_2 vol. gas composition. Each sample was exposed 15 minutes to the plasma and then immediately loaded into an Alliance-Concept DP 650 sputtering machine. Depending on the sample, a thin Ni or Mo layer was deposited on top of the diamond, before being covered by an 80-nm thick Ag or Au layer. A 20-nm thick Cr layer was finally added on top of each sample to act as a transducer. A vacuum level lower than $5 \cdot 10^{-6}$ mbar was maintained during the whole stack deposition process. In addition, Au/(nm-thick Cu)/O:C samples presented in Ref. (14) were reused to measure the influence of ultra-thin interlayers at liquid nitrogen temperature.

The thickness of each layer was measured by X-Ray Reflectivity (XRR), which is highly sensitive to the presence of ultra-thin interlayers inserted between the main metallic layer and its substrate (14). A Panalytical diffractometer (model Empyrean, Malvern Panalytical Ltd.) equipped with a Cu Kα X-Ray source was used for all measurements, which were performed using the ω - 2θ scanning mode with ω angles ranging from 0 to 3°. The experimental curves were fitted by means of the GenX software (15), having as fitting parameters the layers' thickness, density and roughness, as well as possible intermixing between two neighboring layers. The thickness of each interlayer was thus determined with an accuracy better than ± 0.3 nm.

b. Thermal boundary conductance measurement

The TBC of each sample was measured by means of Time Domain Thermoreflectance (TDTR), which consists in a pump-probe experiment (16,17). In a nutshell, a COHERENT Mira 900 operating at a wavelength of 785 nm with a repetition rate of 76 MHz was used to generate the laser pulse train that was split in a pump and a probe part. Over its optical path, the pump was modulated at a frequency of 10.7 MHz using an electro-optic

modulator (EOM, Model 350-160, ConOptics Inc.), which is necessary for lock-in detection. It further went through a mechanical delay stage (M-531-PD1, Physik Instrument GmbH & Co) that allowed sweeping delay times ranging from 0 to 4 ns, which is necessary to record extensive cooling curves. Long (short) pass filters and half wave plates were inserted on both the pump and the probe optical path, respectively, to differentiate them in terms of wavelength and polarization. This so-called “two-tint” technique allows for significant noise reduction. At the end of their respective optical paths, both beams were focused on the same spot of the sample surface using a 10x microscope objective. There, the pump was heating the sample periodically, while the probe was monitoring the change in sample reflectivity, which is linearly dependent on the temperature, provided the temperature increase is not too large. This signal was sent back to a fast-photodiode (Thorlabs DET 10A), before being frequency-filtered, pre-amplified and fed into a ZI-HF2 lock-in amplifier (Zurich Instruments, Zürich, Switzerland).

All measurements were carried out at a target beam power of 7mW together with a target spot size of 4 μm leading to a fluence per pulse of 0.2 mJ/cm^2. The exact value of beam power and spot size was recorded for each experiment using a power meter and a CMOS camera.

For low temperature measurements, sample cooling down to 80 K was achieved using a Janis ST-500 cryostat mounted on a 5-axes stage that was continuously cooled down with liquid nitrogen using a Janis Supertran transfer line, which were both vacuum insulated. The transfer line was pumped down to $1 \cdot 10^{-5}$ mbar on a regular basis before being sealed. The cryostat was pumped down to values better than $1 \cdot 10^{-6}$ mbar, on a daily basis and sealed right before starting experiments to avoid vibrations that would prevent proper measurements. A LakeShore 336 temperature controller was used to achieve precise temperature control over the whole experiment duration.

The TBC values were extracted from the calculated X/Y ratio, with X and Y corresponding to the in-phase and out-of-phase signal extracted from the lock-in amplifier, using the scheme proposed by Cahill (18). The input parameters were the thickness, thermal conductivity, and heat capacity of each layer. The metallic layers' thickness values were taken from XRR measurements. Their thermal conductivity and heat capacity, as well as the diamond heat capacity were taken from the literature (19–23) (see Table I). Finally, the TBC and the diamond thermal conductivity were taken as fitting parameters. The diamond thermal conductivity was not set *a priori*, because it depends on the nitrogen content, which is recognized to vary from one stone to another, as well as within one stone, depending on whether the measurement was taken on a seed part or a secondary growth part (24). As shown in Fig. 1, a good signal to noise ratio, as well as satisfactory fit quality was obtained in all cases.

Table 1: Thermal conductivity and heat capacity values used to extract TBC values out of the X/Y TDTR signal.

Metal	Temperature [K]	Thermal conductivity [W/m·K]	Heat capacity ·10^6 [J/m^{3}K]
Ag	300	429 *	2.47 *
Au	300	317 *	2.49 *
Cr	300	93 *	3.21 *
Mo	300	138 *	2.56 *
Ni	300	91 *	3.95 *
Au	80	320 **	1.96 ***
Cr	80	170 **	0.43 [x]
Cu	80 550 **	1.83 [xx]	

* from (19), ** from (20), *** from (22), [x] from (21) and [xx] from (23).

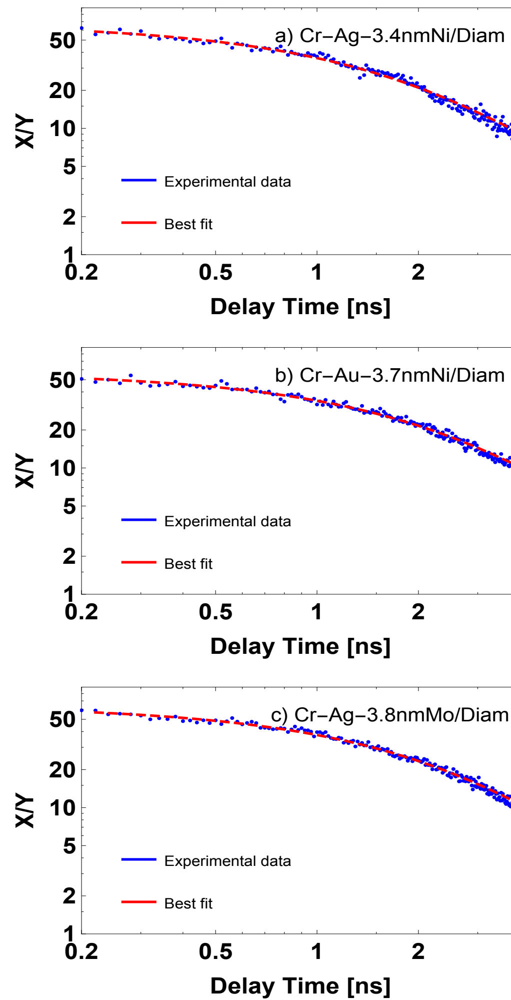

Fig. 1: TDTR raw data recorded for three samples of (a) Ag/(nm-thick Ni)/diamond, (b) Au/(nm-thick Ni)/diamond, and (c) Ag/(nm-thick Mo)/diamond. The continuous lines stand for the best fits.

III. RESULTS

a. TBC at Au/diamond and Ag/diamond interfaces with Ni and Mo interlayer.

The TBC values obtained for the Ag/(nm-thick) Ni/diamond system are shown in Fig. 2. The TBC was observed to increase from 45 MW/m^2K (25) to 177 MW/m^2K when inserting a 1.5 nm Ni interlayer. For larger interlayers, a plateau was reached with an average value of 214 MW/m^2K, i.e. ~75% of the Ni/diamond TBC value of 290 MW/m^2K (25).

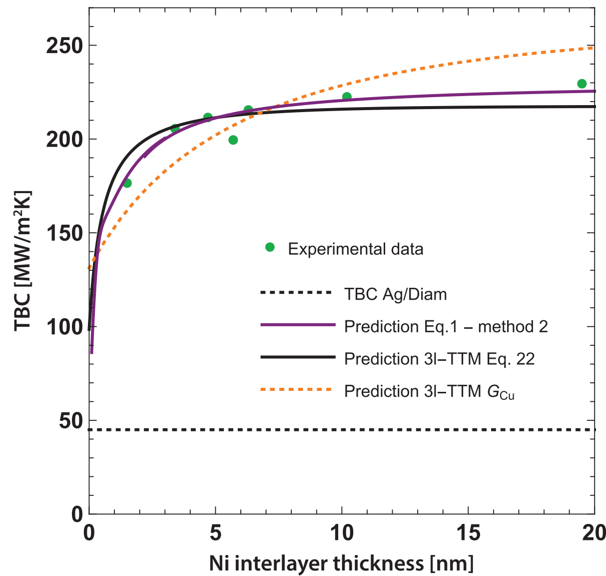

Fig. 2: Influence of a thin Ni interlayer on the TBC at the Ag/O:C interface together with the fits obtained with Eqs. 1 (purple) and 22 (black). The former fit was obtained using method 2, i.e. the best fit was calculated by allowing the Ag/diamond TBC value to vary within 20% of the value found in Ref. (25), while the electron-phonon coupling factor was allowed to vary by a factor of two as compared to the value given in Table 4. Experimental data are expected to be precise to 20%. Errors bars were not included within this graph to facilitate reading.

The TBC values measured for the Au/(nm-thick) Ni/diamond system are given in Fig. 3. The TBC was observed to increase from 76 MW/m^2K (25) to 208 MW/m^2K when inserting a 1.5 nm Ni interlayer. Unlike for the Ag/(nm-thick Ni)/diamond system, no further evolution is observed; the TBC has already reached its plateau value, which falls very close to the one obtained in the Ag/(nm-thick Ni)/diamond system (208 vs. 214 MW/m^2K).

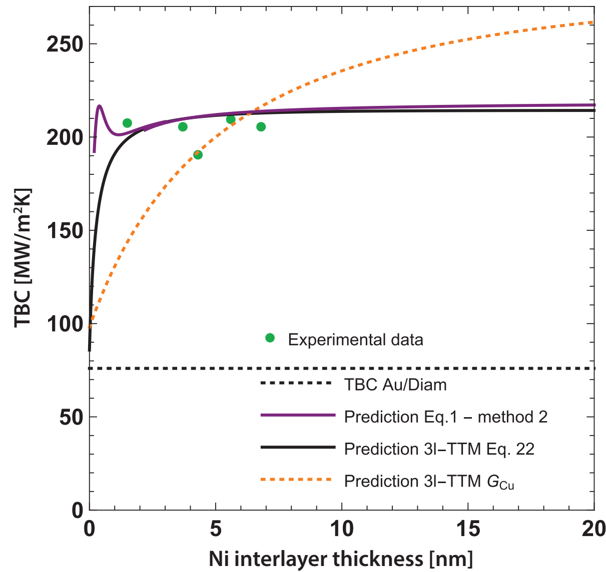

Fig. 3: Influence of a thin Ni interlayer on the TBC at the Au/O:C interface, same comments as for Fig. 2.

Fig. 4 shows the TBC values that were obtained for the Ag/(nm-thick) Mo/diamond system. The thinnest Mo interlayer that could be achieved was 3.8 nm, which is large compared to the thinnest layers obtained for Ni or Cu, which were rather close to 1.5 nm. Consequently, no gradual increase of the TBC with the interlayer thickness could be observed. Instead, a roughly constant value of 189 MW/m^{2}K was reached for all samples tested, i.e. more than 4 times the TBC value measured at the Ag/diamond interface and 85 % of the Mo/diamond TBC value of 220 MW/m^{2}K (25).

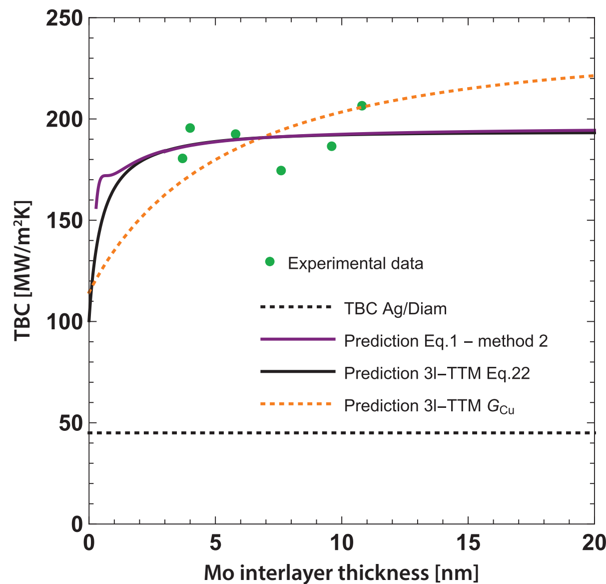

Fig. 4: Influence of a thin Mo interlayer on the TBC at the Ag/O:C interface, same comments as for Fig. 2.

b. TBC at the Au/Si interface at 80K

At 80K, the TBC at the Au/Si interface was measured to be 47 MW/m²K, while it was measured to be 153 MW/m²K at the Cu/Si interface. Figure 5 shows the evolution of the TBC as a function of the copper interlayer thickness. A 1.5 nm interlayer is observed to already have a significant effect on the TBC by increasing it from 47 MW/m²K (Au/Si) to 80 MW/m²K. This value further increases for interlayer thicknesses up to roughly 10 nm. A plateau is then reached with an average TBC value of 125 MW/m²K, which corresponds to 80% of the value achieved at the Cu/Si interface.

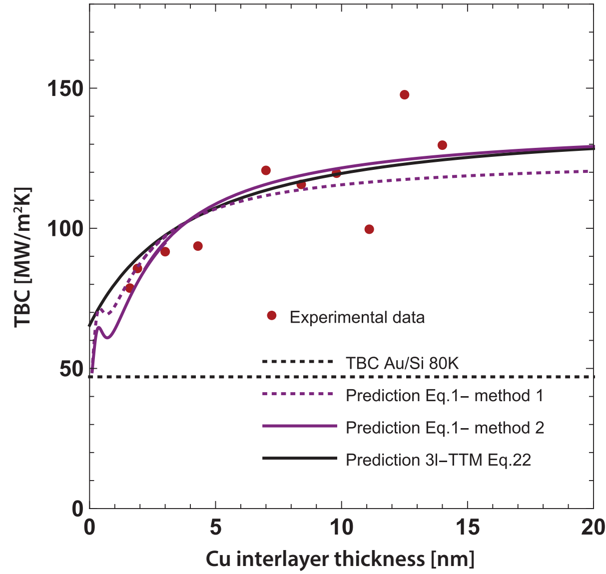

Fig. 5: Influence of a thin Cu interlayer on the TBC at the Au/Si interface measured at 80K together with the fits obtained with Eqs. 1 (dotted purple and purple) and 22 (black). The former fit was obtained using method 2, i.e. the best fit was calculated by allowing the Au/diamond TBC value to vary within 20%, while the electron-phonon coupling factor was allowed to vary by a factor of two as compared to the value given in Table 4. Experimental data are expected to be precise to 20%. Errors bars were not included within this graph to facilitate reading.

IV. DISCUSSION

a. Influence of the interlayer electron-phonon coupling factor on the TBC at metal/dielectric interfaces

Earlier works performed on the influence of a thin interlayer on the TBC at metal/dielectric interfaces used interlayers made of copper (13,14). The TBC was observed to increase monotonically for interlayers up to roughly 10 nm before reaching a plateau at a value that is close to the interlayer/dielectric TBC value (see Fig. 6 to 8, adapted from (14)). Blank and Weber (14) postulated that the TBC dependence on the interlayer thickness can be rationalized assuming that the thermal transport is controlled by three resistances in series, i.e. the metal-metal interfacial resistance $1/h_{ee}$,

the metal-dielectric resistance $1/h_{\mathrm{pp}}$ and a resistance within the interlayer that depends on its electron-phonon coupling factor G and that becomes smaller as the interlayer gets thicker. A resistance in parallel was further added to account for a possible direct coupling between the phonons from the main metallic layer and the substrate. This last contribution is referred as $h_{\mathrm{tunnelling}}$ (13,14). The system total conductance is consequently expressed by Eq. 1.

$$h_{BD} = \left(\frac{1}{h_{\mathrm{ee}}} + \frac{1}{h_{\mathrm{pp}}} + \frac{1}{G \cdot l}\right)^{-1} + h_{tunnelling} \qquad (1)$$

with l the interlayer thickness.

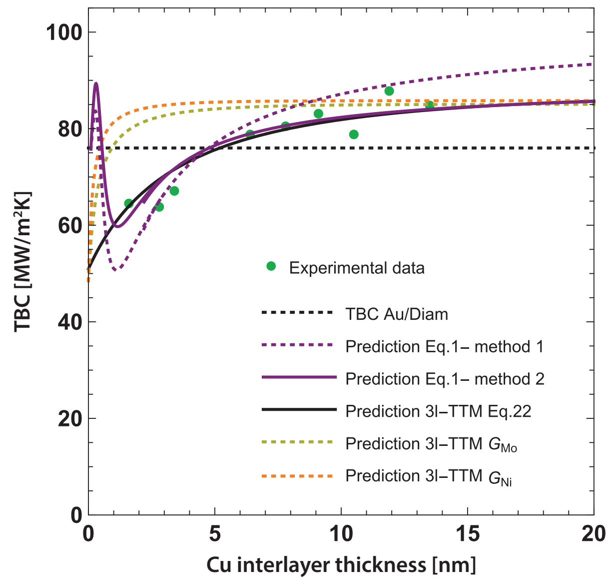

Fig. 6: Influence of a thin Cu interlayer on the TBC at the Au/O:C interface together with the fits obtained with Eqs. 1 (dotted purple and purple) and 22 (black). The dotted purple fit (method 1) was obtained assuming the TBC to be fixed, while the G was fitted without any particular restriction. The solid purple fit was obtained using method 2, i.e. the best fit was calculated by allowing the Au/diamond TBC value to vary within 20% of the value found in Ref. (14), while the electron-phonon coupling factor was set to half of the value given in Table 4. Experimental data are expected to be precise to 20%. Errors bars were not included within this graph to facilitate reading.

We first note that the contribution by phonon tunnelling will decrease rapidly with the interlayer thickness and will be negligible for thicknesses larger than roughly 2 nm. For the leading term in parenthesis of Eq. 1 a value independent of the layer thickness, l, i.e. a plateau in h_{BD}, will be reached when the product of $G{\cdot}l$ gets very large compare to, both, h_{ee} and h_{pp}. The onset of this plateau is hence expected to start at very small interlayer thickness for large interlayer electron-phonon coupling factor and to progressively move towards larger interlayer thickness with decreasing electron-phonon coupling factor. This statement can be critically assessed by comparing the results obtained for

interlayers made of copper, which has a relatively weak electron-phonon coupling factor [G_{Cu} = (5-10)·10^{16} W/m^{3}K (26,27)] to the results obtained for interlayers made of nickel or molybdenum, which have a much stronger electron-phonon coupling constant ($G_{Ni} \approx$ 100·10^{16} W/m^{3}K, $G_{Mo} \approx$ 50·10^{16} W/m^{3}K (26)).

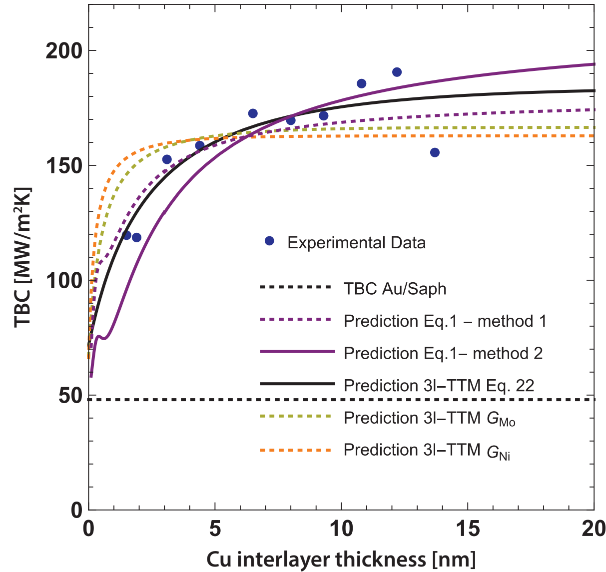

Fig. 7: Influence of a thin Cu interlayer on the TBC at the Au/Al_2O_3 interface, same comments as for Fig. 6.

The TBC measured for 1.5 nm-thick Ni interlayers inserted at the interface between Ag and diamond was shown to be slightly lower than the value measured for 3.4 nm-thick interlayer, although the difference is comparable to the measurement uncertainty. This might indicate the presence of a gradual increase of the TBC over a very limited range of interlayer thicknesses. For interlayers larger than 1.5 nm, a plateau is reached. For Au/(nm-thick Ni)/diamond and Ag/(nm-thick Mo)/diamond samples, such a gradual increase of the TBC could not be observed. The plateau was reached even for the thinnest layer tested. This indicates that the increase of the TBC due to the Ni and Mo interlayers is much more abrupt than the TBC increase due to copper interlayers. This result is in qualitative agreement with the prediction given by Eq. 1.

A quantitative characterization of each system was achieved by fitting the experimental data using Eq. 1. The conductance due to phonons tunnelling from the gold layer was evaluated following the same procedure as the one described in (14). Table 2 summarizes the parameters used.

The metal-metal interfacial conductance h_{ee} was estimated by using the electronic version of the DMM developed by Gundrum *et al.* (30) and expressed by Eq. 2.

$$h_{\rm ee} = \frac{\gamma_{\rm s,1} v_{\rm f,1} \gamma_{\rm s,2} v_{\rm f,2}}{4(\gamma_{\rm s,1} v_{\rm f,1} + \gamma_{\rm s,2} v_{\rm f,2})} T \qquad (2)$$

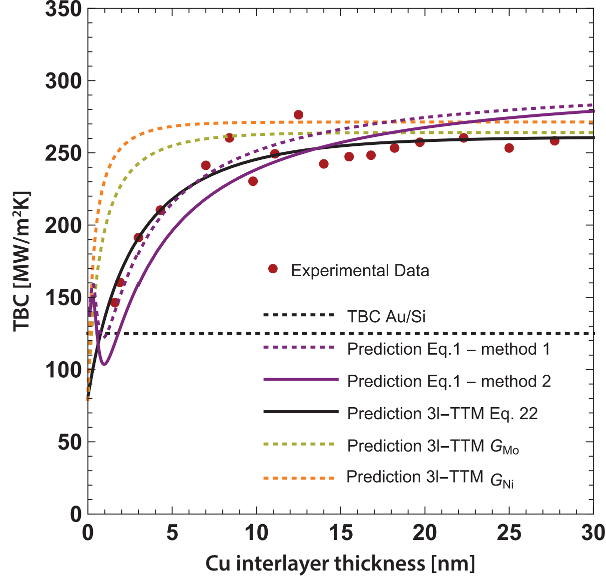

Fig. 8: Influence of a thin Cu interlayer on the TBC at the Au/Si interface, same comments as for Fig. 6.

with γ_s the Sommerfeld constant and v_f the Fermi velocity of the materials of on either side of the interface and T the temperature. Table 3 summarizes the results obtained for the interfaces studied. h_{pp} and G were then extracted by evaluating the contribution of the three conductances in series (h_{ee}, h_{pp} and $G{\cdot}l$) from the experimental data using a best fit procedure. Therefore, h_{pp} values were taken from (25) and allowed to vary within 20%, while G was taken from (26) (cf. Table 3) and allowed to vary by a factor of 2. A variability of 20% for h_{pp} value was allowed because it corresponds to the typical uncertainty attributed to TDTR measurements. As for the G value, the factor of 2 reflects the variability of the values that are typically found in the literature (26,33–35). This procedure (later referred as method 2) is slightly different from the one used in Ref. (14) (later referred as method 1) in which h_{pp} was fixed and the G was fitted without any particular restriction. This modification was necessary to allow for experimental data fitting using the 3l-TTM (see section IV.c.) and thus to allow for a direct comparison between both methods. The results shown in Fig. 6 to 8 were fitted using both methods. Very similar predictions were obtained in both cases. As shown in Fig. 2 to 4, a good fit quality was obtained for all tested systems, which tends to confirm the importance of the interlayer electron-phonon coupling factor in the overall thermal transport at metal/(nm-thick) interlayer/dielectric interfaces.

Table 2 : Parameters used to evaluate the conductance due to phonon tunnelling from the gold layer with ω_{max} the phonons maximum frequency, v_{av} the average sound velocity and $G_{e\text{-}ph,\ metal/diamond}$, the experimental TBC measured at the metal/diamond interface.

Metal	ω_{max} **[THz]** (28)	v_{av} **[m/s]** (29)	$h_{pp,metal\text{-}diamond}$ **[MW/m²K]** (25)
Au	4.7	2128	45
Ag	5.1	2514	75

Table 3: $1/R_{e12}$ values calculated from the electronic equivalent of the DMM for the different metal-metal couples tested.

Metal couple	$\gamma_{s,1}$ [J/m³K] (31)	$v_{f,1}$ x10⁶[m/s] (31)	$\gamma_{s,2}$ [J/m³K] (31)	$v_{f,2}$ x10⁶[m/s] (32)	$h_{ee}=1/R_{e12}$ [GW/m²K]
Ag-Ni	62.8	1.39	1064	0.2	4.6
Au-Ni	71.5	1.4	1064	0.2	5.1
Ag-Mo	62.8	1.39	214	0.9	4.5

b. Limitations of the previously presented model

The underlying picture of heat transfer leading to Eq. 1 is schematically represented in Fig. 9a. The overall drop in temperature across the interface consists of a drop ΔT_{ee}, a drop ΔT_{ep} in the interlayer and a drop ΔT_{pp} at the interface between the interlayer and the dielectric. For simplicity's sake not much heed has been given to the evolution of the electron and phonon temperature in the interlayer. Rather, the difference of these two temperatures, ΔT_{ep}, has been considered constant corresponding to an average over the thickness of the layer. Under this assumption, the heat transferred from the electrons to the phonons is proportional to the thickness of the interlayer and to the temperature difference between electrons and phonons. Since the heat passing through the interface is proportional to the phonon-phonon TBC at the metal dielectric interface and is identical to the heat transferred in the interlayer from the electrons to the phonons, the ratio $\Delta T_{ep}/\Delta T_{pp}$ becomes smaller and smaller with larger interlayer thickness and ΔT_{pp} approaches asymptotically ΔT - ΔT_{ee}, cf. Fig. 9b. In parallel, some phonons tunnel through the interlayer, yet this contribution gets negligible for interlayers thicker than 2 nm.

As such this simple model has two major shortcomings: i) it neglects the heat flux equilibrium and the ensuing evolution of the phonon and electron temperature in the interlayer, ii) it doesn't give any description of the phonon-phonon heat transfer at the main layer/interlayer interface. In order to overcome these shortcomings, we detail in the following a 3l-TTM which takes care of these issues.

c. Two temperatures model for a 3-layers system

In an attempt to provide a more rigorous approach to describe the mechanisms involved in the heat transfer of metal/(nm-thick) interlayer/dielectric system, we develop below the formalism for a 3l-TTM, schematically depicted in Fig. 9c. Similarly to the TTM developed by Madjumdar and Reddy (36), the 3l-TTM presented below assumes that:

1. The heat transport through the metallic layers is due to the electron and phonon gases, as well as to their mutual interactions.
2. The system has reached a steady state.

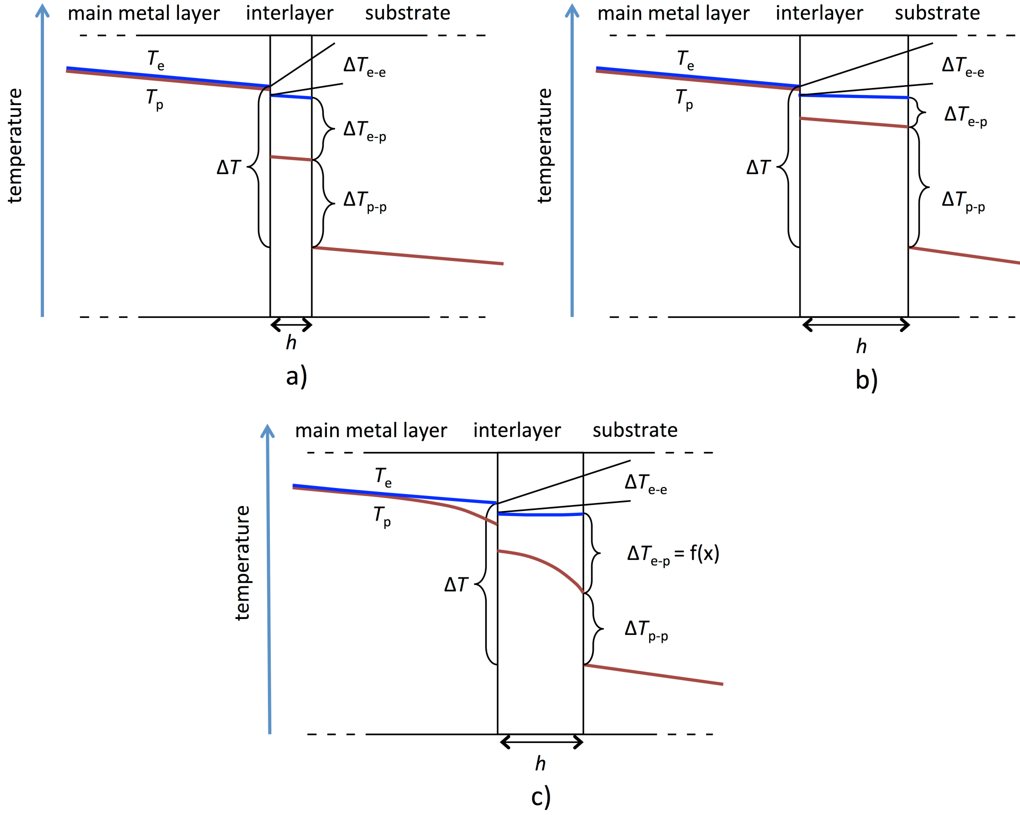

Fig. 9: Schematic temperature profiles predicted by the (a,b) the simplified steady-state model in Eq. (1) and c) the rigorous 3l-TTM model based on Eq. (22). Sketches in a) and b) indicate the difference between the phonon and electron temperatures for different interlayer thicknesses.

After a few hundred picoseconds the temperature distribution in a pump-probe experiment evolves much more slowly than the time constant of equilibration between electron and phonon temperature and hence might be approximated by a steady state treatment.

A schematic of the system is presented in Fig. 10. The electron and phonon temperature inside each layer obey the leading differential equations given by Eq. 3 and 4 (36,37).

$$\frac{d^2T_{ei}}{dx^2} - \frac{G_i}{\kappa_{ei}}\left(T_{ei} - T_{pi}\right) = 0, \tag{3}$$

$$\frac{d^2T_{pi}}{dx^2} + \frac{G_i}{\kappa_{pi}}\left(T_{ei} - T_{pi}\right) = 0, \tag{4}$$

with T being the temperature, G the electron-phonon coupling factor and κ the thermal conductivity. The subscripts i, e and p stand for the layer under consideration, the electrons and the phonons, respectively. The general solutions of Eqs. 3 and 4 for the electron and phonon temperatures are given by

$$T_{ei}(x) = A_i + B_i(x - l_{i-1}) + \frac{\kappa_{ai}}{\kappa_{ei}}\left(C_i \sinh\left(\frac{x-l_{i-1}}{d_i}\right) + D_i \cosh\left(\frac{x-l_{i-1}}{d_i}\right)\right), \tag{5}$$

$$T_{pi}(x) = A_i + B_i(x - l_{i-1}) - \frac{\kappa_{ai}}{\kappa_{pi}}\left(C_i \sinh\left(\frac{x-l_{i-1}}{d_i}\right) + D_i \cosh\left(\frac{x-l_{i-1}}{d_i}\right)\right), \tag{6}$$

where A, B, C and D are constants to be determined for each layer, and

$$d_i^2 = \frac{\kappa_{ai}}{G_i}, \tag{7}$$

$$\frac{1}{\kappa_{ai}} = \frac{1}{\kappa_{ei}} + \frac{1}{\kappa_{pi}}. \tag{8}$$

Taking into account that the heat conduction in the dielectric layer is due to the phonon gas only, its temperature evolution is described by

$$T_3(x) = A_3 + B_3 x. \tag{9}$$

The ten constants involved in Eqs. (5), (6) and (9) are determined by proper boundary conditions at the layer interfaces. Considering that the laser energy is only transferred to the electron gas and that the phonons at the illuminated film surface are insulated from the environment, the boundary conditions at x=0 are given by

$$-\kappa_{e1} \left.\frac{dT_{e1}}{dx}\right]_{x=0} = J, \tag{10}$$

$$\left.\frac{dT_{p1}}{dx}\right]_{x=0} = 0. \tag{11}$$

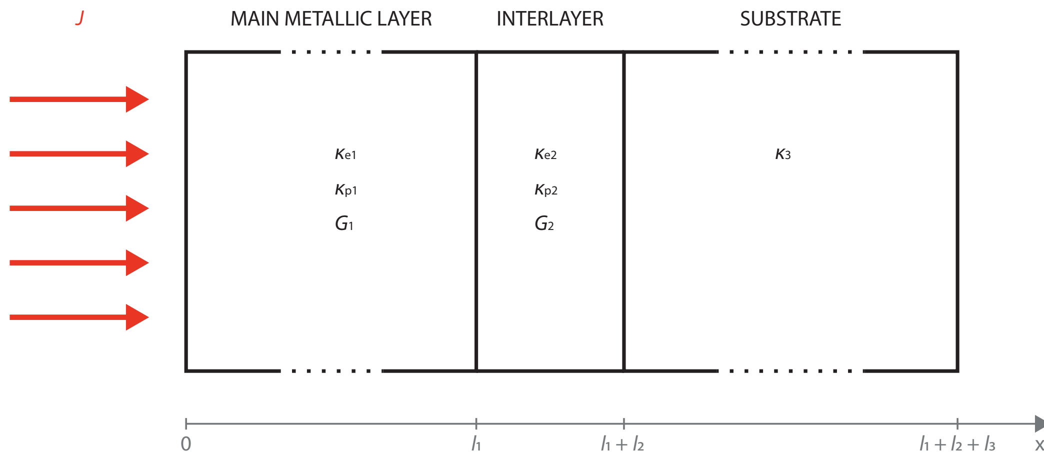

Fig. 10: System considered to develop the 3l-TTM. The heat flux first propagates through the two metallic layers before reaching the dielectric substrate of thermal conductivity κ. Each metallic layer is characterized by its electron (κ_e) and phonon (κ_p) thermal conductivities along with its electron-phonon coupling constant G.

At the interface $x=l_1$ between the main metallic layer and the interlayer, the electrons (phonons) of the main metallic layer transfer their energy to the electrons (phonons) of the interlayer. The electrons and the phonons are both assumed to encounter a certain interfacial resistance. Those conditions combined with the usual requirements for heat flux continuity lead to the following boundary conditions

$$\kappa_{e1}\frac{dT_{e1}}{dx}\bigg]_{x=l_1}=\kappa_{e2}\frac{dT_{e2}}{dx}\bigg]_{x=l_1},\tag{12}$$

$$\kappa_{p1}\frac{dT_{p1}}{dx}\bigg]_{x=l_1}=\kappa_{p2}\frac{dT_{p2}}{dx}\bigg]_{x=l_1},\tag{13}$$

$$(T_{e1}-T_{e2})]_{x=l_1}=-R_{\mathrm{e}12}\kappa_{e2}\frac{dT_{e2}}{dx}\bigg]_{x=l_1},\tag{14}$$

$$(T_{p1}-T_{p2})\big]_{x=l_1}=-R_{\mathrm{p}12}\kappa_{\mathrm{p}2}\frac{dT_{\mathrm{p}2}}{dx}\bigg]_{x=l_1},\tag{15}$$

where $R_{\mathrm{e}12}$ and $R_{\mathrm{p}12}$ are the thermal resistances accounting for the electron-electron and phonon-phonon thermal mismatch at the interface of layers 1 and 2.

At the interface $x=l_1+l_2$ between the interlayer and the substrate, the heat flux transported by electrons into the interlayer is assumed to have been transferred to the phonons of the interlayer, which then transfer their energy to the phonons of the substrate via phonon-phonon interactions. These conditions read, as follows

$$\frac{dT_{e2}}{dx}\bigg]_{x=l_1+l_2}=0,\tag{16}$$

$$\kappa_{p2}\frac{dT_{p2}}{dx}\bigg]_{x=l_1+l_2}=\kappa_3\frac{dT_3}{dx}\bigg]_{x=l_1+l_2},\tag{17}$$

$$(T_{p2}-T_3)\big]_{x=l_1+l_2}=-R_{23}\kappa_3\frac{dT_3}{dx}\bigg]_{x=l_1+l_2}.\tag{18}$$

Finally, at the bottom at $x=l_1+l_2+l_3$ of the substrate, the temperature is assumed to remain constant and equal to room temperature, that is to say

$$T_3]_{x=l_1+l_2+l_3}=T_0\tag{19}$$

Equations 10 to 19 allow calculating all the constants involved Eqs. 5, 6 and 9. The $h_{\mathrm{BD}}=1/R_{\mathrm{EFF}}$ of the three-layer system is then determined through its effective thermal resistance defined by

$$T(l_1+l_2)-T_3(l_1+l_2)=R_{EFF}\cdot J, \tag{20}$$

where $T(l_1+l_2)$ is the common linear extrapolation of the electron and phonon temperatures of the interlayer, and is therefore given by

$$T(l_1+l_2)=A_2+B_2\cdot l_2. \tag{21}$$

By inserting Eqs. 5,6 and 9 into Eq. 21 and assuming that the first layer is much thicker than its electron-phonon coupling distance (l_1/d_1>>1), one obtains

$$R_{EFF}=R_{23}+\frac{\kappa_{a2}}{\kappa_{p2}}\left(\frac{a-b}{c}\right), \tag{22}$$

where

$$a=\left(\frac{d_1}{\kappa_{a1}}\frac{\kappa_{e2}}{\kappa_2}+\frac{\kappa_{a2}}{\kappa_{p2}}(R_{e12}+R_{p12})\right)\cosh\left(\frac{l_2}{d_2}\right)+\frac{d_2}{\kappa_{p2}}\sinh\left(\frac{l_2}{d_2}\right), \tag{23}$$

$$b=\frac{1}{\kappa_2}\left(R_{e12}\kappa_{e2}-R_{p12}\kappa_{p2}+\alpha_{21}d_1\right), \tag{24}$$

$$c=\frac{\kappa_{a2}}{d_2}\left(\frac{d_1}{\kappa_{a1}}+R_{e12}+R_{p12}\right)\sinh\left(\frac{l_2}{d_2}\right)+\cosh\left(\frac{l_2}{d_2}\right), \tag{25}$$

$$\alpha_{21}=\frac{\kappa_{e_1}}{\kappa_{e_2}}-\frac{\kappa_{p_1}}{\kappa_{p_2}}. \tag{26}$$

The parameters required to compare the prediction of the model in Eq. 22 to the experimental data are κ_e, κ_p and G of each layer, as well as R_{e12}, R_{p12} and R_{23}. The values of κ_e, κ_p and G are tabulated in Table 4, while those of R_{e12} and R_{p12} are summarized in Table 5. All R_{23} values were taken from Ref. (25), κ_e was calculated by subtracting the lattice thermal conductivity κ_p from the thermal conductivity reported in Table 1 and G was taken from the work reported by Lin *et al.* (26), assuming $T_e \approx 300$ K. R_{e12} was estimated by using the procedure described in section IV. a, while R_{p12} was calculated through the standard DMM involving a Debye linear dispersion relation.

Table 4: Electronic thermal conductivity, lattice thermal conductivity and electron phonon coupling factor at T_e=300 K for all the metals tested.

	Ag	Au	Cu	Mo	Ni	Si	Al_2O_3	C (diamond)
κ_e [W/m·K]	424	314	384	105	66	-	-	-
κ_p [W/m·K]	5.2 *	2.6 *	17*	33**	25*	124	35	1500
G 10^{16} [W/m^{3}K]	2.5	2.6	10***	48	100	-	-	-

* from (36); ** from (37) and ***from (27)

Table 5: $1/R_{e12}$ values calculated from the electronic equivalent of the DMM and $1/R_{p12}$ values calculated from the DMM for the different metal-metal couples tested at 300 K.

Metal couple	$1/R_{e12}$ [GW/m^{2}K]	$1/R_{p12}$ [GW/m^{2}K]
Au-Cu	4.5	0.24
Ag-Ni	4.6	0.25
Au-Ni	5.1	0.15
Ag-Mo	4.5	0.22

The fitting of Eq. 22 to the experimental data was performed by allowing the TBC values to vary within 20% of the ones given in Ref. (25), while the electron-phonon coupling factor was allowed to vary by a factor of 2 as compared to the value given in Table 4. Figures 2 to 4 and 6 to 8 display the fits of Eqs. 1 and 22 along with the experimental data. For systems with a Cu interlayer, the fits obtained by assuming the interlayer to have the same electron-phonon coupling factor as Mo and Ni are further provided for comparison. Similarly, for systems with Mo or Ni interlayers, fits that assume the interlayer to have the same electron-phonon coupling factor as copper are provided for comparison. An accurate fit is thus obtained for all cases, with the predictions of both Eqs. 1 and 22 falling close to each other. The fits obtained using larger (for Cu interlayers) and smaller (for Mo and Ni interlayers) electron-phonon coupling factors further show features that are completely different from the experimental data, which confirms that the overall TBC is controlled by the interlayer electron-phonon coupling factor.

Figure 11 details this last statement by means of a temperature profile obtained for both a thin and a large interlayer that has either a small (5.5 MW/m^{3}K) or a large (55 MW/m^{3}K) electron-phonon coupling factor. As expected, non-equilibrium between electrons and phonons is larger in thin interlayers, resulting in lower TBC values. A large electron-phonon coupling factor is shown to be an efficient way to reduce non-equilibrium even in very thin interlayers, which is consistent with the observation that the interlayer thickness required for the TBC to reach a plateau decreases with increasing the electron-phonon coupling factor.

d. Low-temperature data on Au/(nm-thick) Cu/Si interfaces

As expected at such a temperature, the TBC values are lower by a factor of roughly 2 as compared to room temperature values (see Fig. 8). Interestingly enough, however, the overall dependence of the TBC on the interlayer thickness is observed to be very similar at 80K and at room temperature, i.e. the TBC increases monotonically over roughly 10 nm before reaching a plateau.

A quantitative analysis of these data was achieved using the fitting models described by Eqs. 1 and 22. At 80K, the parameters necessary to perform the fits were determined as follows:

- The thermal resistance due to the electron temperature mismatch at the Au/Cu interface R_{e12} (for Eq. 22)=1/h_{ee} (in Eq. 1) was evaluated be 1.02 GW/m²K using Eq. 2.
- The thermal resistance due to the phonon temperature mismatch at the Au/Cu interface R_{p12} was evaluated to be 0.15 GW/m²K using a standard DMM with a linear Debye dispersion relationship with the sound velocities extracted from the elastic constants measured at 80K (38,39).
- The phonon thermal conductivity is expected to be inversely proportional to the absolute temperature and was thus calculated from room temperature values and set to 9.8 and 63 W/mK for gold and copper respectively.
- The electron thermal conductivity was calculated by subtracting the phonon thermal conductivity from the thermal conductivity given in Table 1.

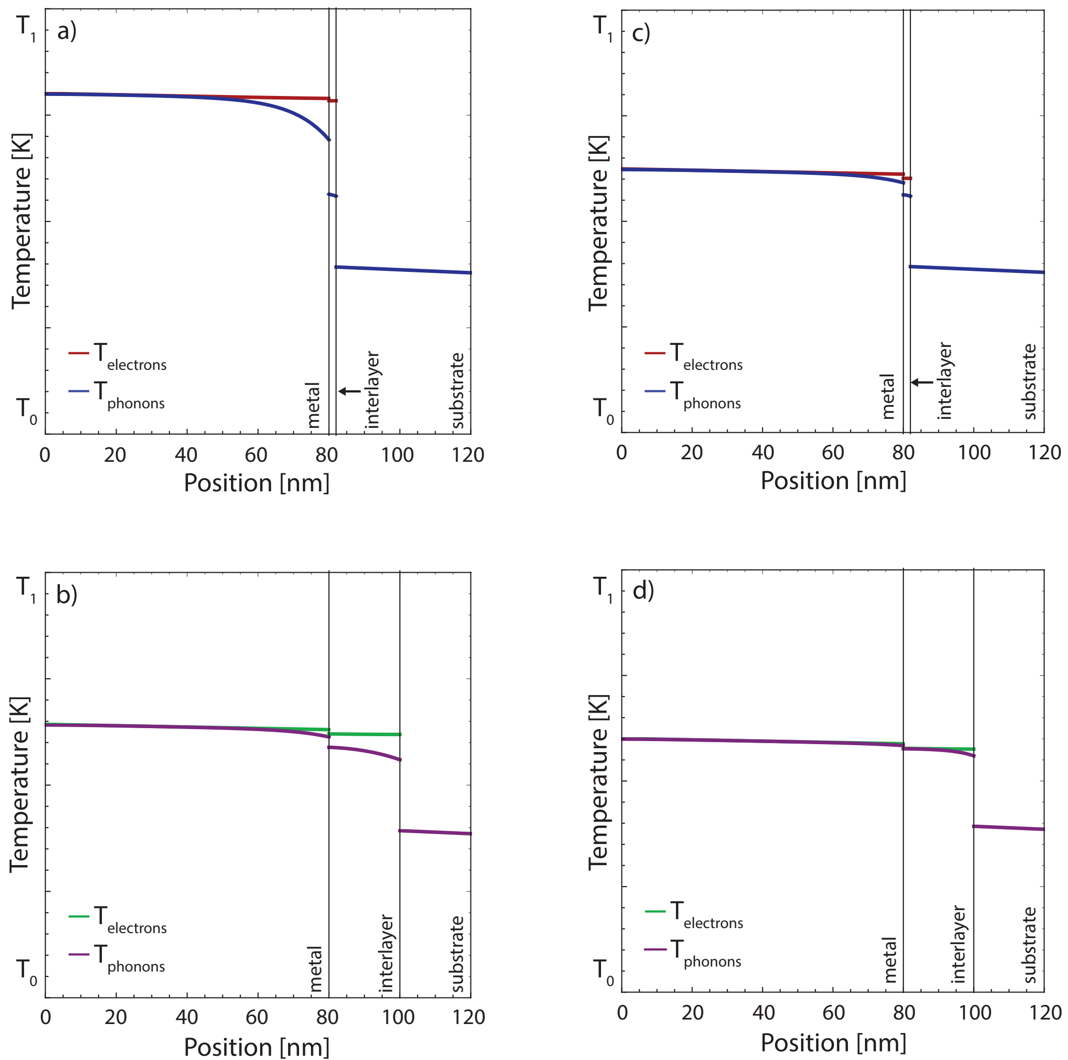

Fig. 11: Temperature profiles predicted by the 3l-TTM for a system with an interlayer characterized by (d, G)= a) (2 nm, $5{\cdot}10^{16}$ MW/m³K), b) (20 nm, $5{\cdot}10^{16}$ MW/m³K) c) (2 nm, $50{\cdot}10^{16}$ MW/m³K), and d) (20 nm, $50{\cdot}10^{16}$ MW/m³K). All calculations were done with the same values of T_0 and T_1 driving the heat flux J.

According to basic theory (40) on electron-phonon heat transfer, the coupling factor G should be independent of temperature for phonon and electron temperatures lower, or on the order of, the Debye-temperature of the lattice. The 3l-TTM and the simpler model given by Eq. 1 would hence suggest that the interlayer thickness l_{trans} at which the TBC should reach a stable value should scale roughly as

$$l_{\text{trans}} \propto \frac{h_{\text{pp}}}{G} \tag{27}$$

Since h_{pp} decreases by a factor of about 2 between 300 K and 80 K the basic model given by Eq. 1 would predict the transition to happen over a thickness range smaller by the same factor. The 3l-TTM can also account for changes in phonon conductivity, in h_{ee}, and in temperature distribution, making it more complete. For the room-temperature value of G, the 3l-TTM also predicts a steeper rise in TBC with increasing interlayer thickness at 80 K than for 300 K. This, however, would be qualitatively at odds with the observed changes for the Au/(nm-thick) Cu/Si system studied at both 300 K and 80 K, cf. Fig. 5 and 8, where, experimentally, the transition seems to take place over even a slightly larger thickness range at 80 K than at 300K. The predictions of the 3l-TTM with identical electron-phonon coupling factor for both temperatures are also indicated. In order to make the 3l-TTM model fit the experimental evolution one would have to reduce the electron-phonon coupling constant by a factor of roughly 2. This stands to reason, since comparable changes in electron phonon coupling factors have experimentally been observed between 300 K and 100 K for gold and silver by Groeneveld *et al.* (41) and are in agreement with time dependent Density Functional Theory modeling for gold by Zhou *et al.* (42). In the absence of comparable data for Cu, yet in view of the similarity of the electron structure of Ag, Au, and Cu, we infer that copper would experience a similar reduction in electron-phonon coupling factor.

Since the electron-phonon coupling factor had already been determined by the fit of the data measured at 300 K, fitting of the experimental data was performed by setting the electron-phonon coupling constant to half its room temperature value and allowed the intrinsic TBC at the interface between metal interlayer and dielectric to vary by 20%. The results obtained are plotted with the experimental results in Fig. 5, showing good agreement.

e. On the utility of nm-thick interlayers in real applications

In this section, we discuss the influence of an interlayer on the thermal transport of a metal/dielectric system in its globality. This work shows that a thin interlayer can significantly enhance the TBC at the interface between the metallic stack and the dielectric. On the other hand, it is responsible for an additional thermal resistance that scales with its thickness and the inverse of its thermal conductivity. To account for these two opposite trends, the overall thermal boundary conductance $\text{TBC}_{\text{global}}$ of the Au/(nm-thick Cu)/Si system was evaluated assuming that the interface was composed of both the interlayer and the interlayer/dielectric interface, which corresponds to the configuration II in Fig. 12. $\text{TBC}_{\text{global}}$ was then observed to increase before reaching a

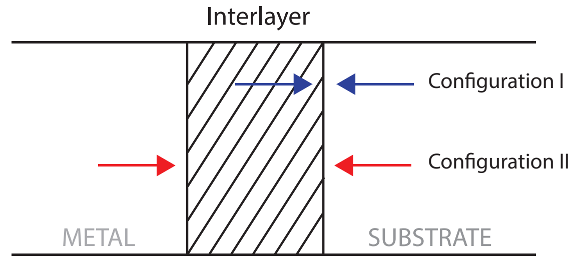

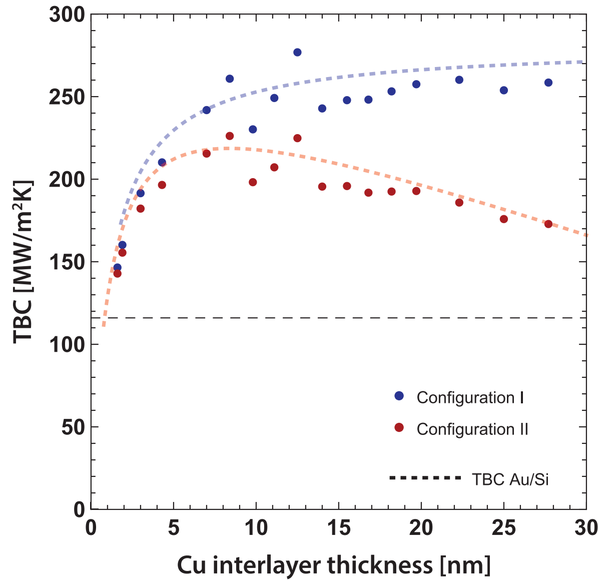

Fig. 12: Evolution of the TBC of an Au/Cu/Si sample as a function of the thickness of its Cu interlayer. The dots stand for the representative experimental data, while the blue and red dashed lines are eye guides related to the configurations I and II, respectively.

maximum at 220 MW/m^2K that is located at the beginning of the TBC plateau. In this region, the increase in the TBC dominates over the temperature drop within the interlayer, which is very small. For thicker layers, the TBC becomes constant, while the temperature drop within the interlayer increases, which results in a decrease of TBC_{global}. The most efficient design for heat transport is thus achieved for interlayers that have a thickness that corresponds to the beginning of the plateau. The measurements performed, however, highlight that the range of thicknesses over which the interlayer is beneficial is relatively large, since TBC_{global} is larger than the TBC at the Au/Si interface for all the thicknesses tested.

V. CONCLUSION

Ni and Mo nanometric interlayers have been shown to significantly increase the TBC of Ag/O:C and Au/O:C interfaces, through values that do not evolve much with the interlayer thickness. The TBC of both systems reaches a plateau at a value much higher than their corresponding TBC without interlayer, but somewhat below the ones of Ni/O:C and Mo/O:C. By contrast, the TBC of Au/(nm-thick Cu)/dielectric systems has been shown to monotonically increase with the interlayer thickness over about 10 nm

before reaching a plateau, due to the relatively weaker electron-phonon coupling factor of Cu with respect to that of Mo and Ni. Furthermore, the comparison of the predictions of a three-layer two-temperature model with data measured at low temperature, suggest that the electron-phonon coupling factor of Cu is reduced by roughly a factor of two, when its temperature drops down from 300 K to 80 K.

ACKNOWLEDGEMENTS
The authors are grateful to the SNSF (Project No 200021_149290) for its financial support and to Prof. O. Martin from the Nanophotonics and Metrology Laboratory (NAM, EPFL), for providing the laser source. Drs. A. Magrez and C. Monachon from the iPhys platform (EPFL) are warmly thanked for their support with the Empyrean diffractometer and for having provided the code to analyse the TDTR data, respectively.

References:

1. Lyeo, H. K., Cahill, D. G., Thermal conductance of interfaces between highly dissimilar materials, *Physical Review B*, 73(14) (2006), 144301, DOI: 10.1103/PhysRevB.73.144301
2. Chen, G., Heat transfer in micro-and nanoscale photonic devices, *Annual Review of Heat Transfer*, 7(7) (1996), 1-57, DOI: 10.1615/AnnualRevHeatTransfer.v7.30
3. Monachon, C., Weber, L., Dames, C., Thermal boundary conductance: A materials science perspective, *Annual Review of Materials Research*, 46 (2016), 433-463, DOI: 10.1146/annurev-matsci-070115-031719
4. Monachon, C., Weber, L., Influence of diamond surface termination on thermal boundary conductance between Al and diamond, *Journal of Applied Physics*, 113(18) (2013), 183504, DOI: 10.1063/1.4804061
5. Oh, D. W., Kim, S., Rogers, J. A., Cahill, D. G., Sinha, S., Interfacial thermal conductance of transfer-printed metal films, *Advanced Materials*, 23(43) (2011), 5028-5033, DOI: 10.1002/adma.201102994
6. Collins, K. C., Chen, S., Chen, G., Effects of surface chemistry on thermal conductance at aluminum–diamond interfaces, *Applied Physics Letters*, 97(8) (2010), 083102, DOI: 10.1063/1.3480413
7. Hopkins, P. E., Phinney, L. M., Serrano, J. R., Beechem, T. E., Effects of surface roughness and oxide layer on the thermal boundary conductance at aluminum/silicon interfaces, *2010 14th International Heat Transfer Conference*, (2010), American Society of Mechanical Engineers, DOI: 10.1115/IHTC14-22268
8. Duda, J. C., Hopkins, P. E., Systematically controlling Kapitza conductance via chemical etching, *Applied Physics Letters*, 100(11) (2012), 111602, DOI: 10.1063/1.3695058
9. Ih Choi, W., Kim, K., Narumanchi, S., Thermal conductance at atomically clean and disordered silicon/aluminum interfaces: A molecular dynamics simulation study, *Journal of Applied Physics*, 112(5) (2012), 054305, DOI: 10.1063/1.4748872
10. Schmidt, A. J., Collins, K. C., Minnich, A. J., Chen, G., Thermal conductance and phonon transmissivity of metal–graphite interfaces, *Journal of Applied Physics*, 107(10) (2010), 104907, DOI: 10.1063/1.3428464
11. Duda, J. C., Yang, C. Y., Foley, B. M., Cheaito, R., Medlin, D. L., Jones, R. E., Hopkins, P. E., Influence of interfacial properties on thermal transport at gold: silicon contacts, *Applied Physics Letters*, 102(8) (2013), 081902, DOI: 10.1063/1.4793431
12. Wang, Y., Lu, Z., Roy, A. K., Ruan, X., Effect of interlayer on interfacial thermal transport and hot electron cooling in metal-dielectric systems: An electron-phonon coupling perspective, *Journal of Applied Physics*, 119(6) (2016), 065103, DOI: 10.1063/1.4941347
13. Jeong, M., Freedman, J. P., Liang, H. J., Chow, C. M., Sokalski, V. M., Bain, J. A., Malen, J. A., Enhancement of thermal conductance at metal-dielectric interfaces using subnanometer metal adhesion layers, *Physical Review Applied*, 5(1) (2016), 014009, DOI: 10.1103/PhysRevApplied.5.014009
14. Blank, M., Weber, L., Influence of the thickness of a nanometric copper interlayer on Au/dielectric thermal boundary conductance, *Journal of Applied Physics*, 124(10) (2018), 105304, DOI: 10.1063/1.5030049
15. Björck, M., Andersson, G., GenX: an extensible X-ray reflectivity refinement program utilizing differential evolution, *Journal of Applied Crystallography*, 40(6) (2007), 1174-1178, DOI: 10.1107/S0021889807045086
16. Kang, K., Koh, Y. K., Chiritescu, C., Zheng, X., Cahill, D. G., Two-tint pump-probe measurements using a femtosecond laser oscillator and sharp-edged optical filters, *Review of Scientific Instruments*, 79(11) (2008), 114901, DOI: 10.1063/1.3020759

17. Monachon, C., Thermal boundary conductance between metals and dielectrics, PhD Thesis N° 5872, *EPFL*, (2013), DOI: 10.5075/epfl-thesis-5872
18. Cahill, D. G., Analysis of heat flow in layered structures for time-domain thermoreflectance, *Review of scientific instruments*, 75(12) (2004), 5119-5122, DOI: 10.1063/1.1819431
19. Rumble, J., CRC handbook of chemistry and physics, *CRC press*, (2017), ISBN: 978-1498784542
20. Powell, R. L., Blanpied, W. A., Thermal conductivity of metals and alloys at low temperatures: a review of the literature (No. NBS-CIRC-556), *National Bureau of Standards Gaithersburg MD*, (1954)
21. Anderson, C. T., The Heat Capacities of Chromium, Chromic Oxide, Chromous Chloride and Chromic Chloride at Low Temperatures1, *Journal of the American Chemical Society*, 59(3) (1937), 488-491, DOI: 10.1021/ja01282a019
22. Takahashi, Y., Akiyama, H., Heat capacity of gold from 80 to 1000 K, *Thermochimica acta*, 109(1) (1986), 105-109, DOI: 10.1016/0040-6031(86)85012-2
23. White, G. K., Collocott, S. J., Heat capacity of reference materials: Cu and W., *Journal of physical and chemical reference data*, 13(4) (1984), 1251-1257, DOI: 10.1063/1.555728
24. Yamamoto, Y., Imai, T., Tanabe, K., Tsuno, T., Kumazawa, Y., Fujimori, N., The measurement of thermal properties of diamond, *Diamond and Related Materials*, 6(8) (1997), 1057-1061, DOI: 10.1016/S0925-9635(96)00772-8
25. Blank, M., Weber, L., Towards a coherent database of thermal boundary conductance at metal/dielectric interfaces, *Journal of Applied Physics*, 125(9) (2019), 095302, DOI: 10.1063/1.5085176
26. Lin, Z., Zhigilei, L. V., Celli, V., Electron-phonon coupling and electron heat capacity of metals under conditions of strong electron-phonon nonequilibrium, *Physical Review B*, 77(7) (2008), 075133, DOI: 10.1103/PhysRevB.77.075133
27. Elsayed-Ali, H. E., Norris, T. B., Pessot, M. A., Mourou, G. A., Time-resolved observation of electron-phonon relaxation in copper, *Physical Review Letters*, 58(12) (1987), 1212, DOI: 10.1103/PhysRevLett.58.1212
28. Dederichs, P. H., H. Schober, David J. Sellmyer, Metals: Phonon States, Electron States and Fermi Surfaces, *Springer-Verlag*, (1981), ISBN: 978-3-540-09774-7
29. Martienssen, W., Warlimont, H. (Eds.), *Springer handbook of condensed matter and materials data*, Springer Science & Business Media, (2006), ISBN: 3-540-44376-2
30. Gundrum, B. C., Cahill, D. G., Averback, R. S., Thermal conductance of metal-metal interfaces, *Physical Review B*, 72(24) (2005), 245426, DOI: 10.1103/PhysRevB.72.245426
31. Kittel, C., Introduction to solid state physics, *John Wiley & Sons. Inc.*, New York, (2005), ISBN: 0-471-41526-X
32. Gall, D., Electron mean free path in elemental metals, *Journal of Applied Physics*, 119(8) (2016), 085101, DOI: 10.1063/1.4942216
33. Hohlfeld, J., Wellershoff, S. S., Güdde, J., Conrad, U., Jähnke, V., Matthias, E., Electron and lattice dynamics following optical excitation of metals, *Chemical Physics*, 251(1-3) (2000), 237-258, DOI: 10.1016/S0301-0104(99)00330-4
34. Wellershoff, S. S., Gudde, J., Hohlfeld, J., Muller, J. G., Matthias, E., Role of electron-phonon coupling in femtosecond laser damage of metals, in *High-Power Laser Ablation* (Vol. 3343, pp. 378-388), International Society for Optics and Photonics, (1998), DOI: 10.1117/12.321573
35. Beaurepaire, E., Merle, J. C., Daunois, A., Bigot, J. Y., Ultrafast spin dynamics in ferromagnetic nickel, *Physical review letters*, *76*(22) (1996), 4250, DOI: 10.1103/PhysRevLett.76.4250
36. Majumdar, A., Reddy, P., Role of electron–phonon coupling in thermal conductance of metal–nonmetal interfaces, *Applied Physics Letters*, 84(23) (2004), 4768-4770, DOI: 10.1063/1.1758301
37. Ordonez-Miranda, J., Alvarado-Gil, J. J., Yang, R., The effect of the electron-phonon coupling on the effective thermal conductivity of metal-nonmetal multilayers, *Journal of Applied Physics*, 109(9) (2011) 094310, DOI: 10.1063/1.3585824.
38. Neighbours, J. R., Alers, G. A., Elastic constants of silver and gold, *Physical Review*, 111(3) (1958), 707, DOI: 10.1103/PhysRev.111.707
39. Overton Jr, W. C., Gaffney, J., Temperature variation of the elastic constants of cubic elements. I. Copper, *Physical Review*, 98(4) (1955), 969, DOI: 10.1103/PhysRev.98.969
40. Kaganov, M. I., Lifshitz, E. M., Tanatarov, L. V., Relaxation between electrons and the crystalline lattice, *Journal of Experimental and Theoretical Physics*, 4 (1957), 173-178
41. Groeneveld, R. H., Sprik, R., Lagendijk, A., Femtosecond spectroscopy of electron-electron and electron-phonon energy relaxation in Ag and Au, *Physical Review B*, 51(17) (1995), 11433, DOI: 10.1103/PhysRevB.51.11433
42. Zhou, X., Li, L., Dong, H., Giri, A., Hopkins, P. E., Prezhdo, O. V., Temperature Dependence of Electron–Phonon Interactions in Gold Films Rationalized by Time-Domain Ab Initio Analysis, *The Journal of Physical Chemistry C*, 121(32) (2017), 17488-17497, DOI: 10.1021/acs.jpcc.7b05211